Proceedings of ASME Turbo Expo 2011
GT2011
June 6-10, 2011, Vancouver, British Columbia, Canada

GT2011-45081

DRY-FRICTION WHIP AND WHIRL PREDICTIONS FOR A ROTOR-STATOR MODEL WITH RUBBING CONTACT AT TWO LOCATIONS

Dara W. Childs
Turbomachinery Laboratory,
Texas A&M University,
College Station, TX 77843 USA
dchilds@tamu.edu

Dhruv Kumar
Graduate Research Assistant
Texas A&M University
College Station, TX 77845
logic87@neo.tamu.edu

ABSTRACT

The present work investigates the phenomena of whip and whirl for a rigid rotor contacting at two bearing locations. The idea originated with a paper by Clark et al. in 2009 on an anemometer undergoing dry friction whip and whirl. The anemometer rotor was supported by two Teflon® bushings within an elastically supported housing. The dry-friction forces arose at the bushings.

Prior models for dry friction whirl and whip have considered rub at one non-support location. The present analytical model consists of a rigid rotor connected to a rigid stator at two rubbing contact locations. Analytical solutions are developed for the following normal reaction forces at the contact locations: (1) In phase, and (2) 180 degrees out of phase. Analytical solutions are only possible for the same *RCl* (Radius to Clearance ratio) at the two rub locations and define regions where dry-friction whirl is possible plus indication possible boundaries between whirl and whip. These solutions are similar to Black's in 1968.

A flexible-rotor/flexible-stator model with nonlinear connections at the bearings was developed to more correctly establish the range of possible solutions. The nonlinear connections at the rub surface are modeled using Hunt and Crossley's 1975 contact model with coulomb friction. Dry friction simulations are performed for the following rotor center of gravity (C.G.) configurations: (1) Centered, (2) ¾ contact-span location and (3) Overhang location outside the contacts.

Results from the in-phase analytical solutions and the nonlinear simulations agree to some extent with the rotor mass centered and at ¾ location in that whirl-to-whip transitions occur near the pinned rotor-stator bounce frequency. For the overhung mass case, the nonlinear simulation predicts whip at different frequencies for the two contact locations. Neither analytical solution modes predicts this outcome. No out-of-phase solutions could be obtained via time-transient simulations.

Dry-friction whirling is normally characterized as supersynchronous precession with a precession frequency equal to running speed times *RCl*. Simulation predictions for models with different *RCl mimic* whirling. Simulation predictions show increasing backward precessional (*BP*) frequency with increasing rotor speeds. However, individual contact velocities show slipping at all conditions. Slipping is greater at one location than the other, netting a "whirl-like" motion. For the overhung model with different *RCl* ratios, apart from whipping at different frequency the two contacts also whirl at different frequencies corresponding to the *RCl* at the respective contacts.

Simulations predict a different running speed for the "jump up" in precession frequency associated with a transition from whirl-to-whip with increasing running speed than for the jump-down in precession frequency for whirl-to-whip in a speed-decreasing mode,

INTRODUCTION

In 1926, Newkirk [1] documented the first case of dry friction whip and whirl. Dry-friction whirl is "tracking" super-synchronous precessional motion at a precession frequency that equals running speed ω times the radius-to-clearance ratio (*RCl*). Whirl normally involves rolling-without-slipping rotor motion at the rotor-stator contact surface. Whip is supersynchronous precession at the combined (pinned) rotor-stator natural frequency, which does not vary with changes in ω. In 1967-1968, Black [2,3] presented the first model and results predicting possible regions of dry-friction whirl, producing characteristic U-shaped curves for the level of Coulomb friction that is required to support whirl. In 1990, Crandall [4] used a Föppl-Jeffcott rotor model contacting an elastically-supported, point-mass stator to obtain results very similar to Black's.

Experiments by Lingener [5] and Choi [6], supported Black and Crandall's predictions. Lingener's test rig used a flexible rotor supported by ball bearings with rubbing contact at a shiftable position between the bearings. The brass stator was elastically supported to ground, and the support stiffness could be varied. His results supported the Black-Crandall predictions; specifically, whirl could be induced by impacts at precession frequencies between the rotor's lowest natural frequency and the rotor-stator pinned natural frequency. For higher speeds that would have induced higher precession frequencies, the precession frequency stopped tracking and remained at the rotor-stator natural frequency; i.e., whip motion. Lingener's rotor could not traverse through the first whip region to reach a higher whirl regime; however, Choi's could, thus validating Black's prediction of a possible return to whirl after crossing a whip regime.

Test results from Bartha [7] and Yu et al. [8] seemed to contradict the Black-Crandall results. They cite differences between whirl ranges predicted by Black versus those achieved experimentally. In 2007, Childs and Bhattacharya [9] revisited Black's model to review his approach in regard to result of Yu et al. and Bartha. They used accurate flexible-rotor models for the test rigs, versus the simplified Föppl-Jeffcott models of Black-Crandall and obtained predictions that agree well with measurements.

Wilkes et al. [10] report on a whip-whirl test rig that demonstrated multi-mode dry-friction whip and whirl modes. The rig produced whip and whirl by inducing rubbing contact at the end of a test rotor. The contact-point bushing supported one end of the rotor; a ball-bearing supported the other end. The test-rig's drive system could produce accurate acceleration and deceleration profiles while sustaining dry-friction instabilities. Multiple whirl-whip regions were produced within the test rig's speed range. Analysis of experimental data showed: (1) The rotor speed was increased and decreased through regions characterized by whip, terminating with jumps to different whirl/whip frequencies for speed-up and speed-down cases. Hence, whip and whirl regions were not solely defined by rotor speed. (2) Observed whirl frequencies were roughly proportional to the radius-to-clearance (*RCl*) ratio at the contact location. (3) Measurements were in reasonable agreement with predictions from a nonlinear time-transient simulation model incorporating flexible-rotor/flexible-stator models with a nonlinear contact model after Hunt and Crossley [11].

In 2009, Clark et al. [12] reported on troubles with one of their company's (NRG systems) anemometer. In 2006, one model started exhibiting slowdown. NRG launched a test program using a video camera to record the tip motion of the rotating anemometer head. The faulty sensors exhibited a "spirograph" motion, which produced a dominant vibration frequency separate from rotation speed. NRG personnel diagnosed the spirograph motion as dry-friction whip and whirl. They contacted the first author who confirmed their diagnosis and worked with NRG personnel to achieve a solution.

The anemometer has a copper shaft supporting its over-hung bladed hub. The rotor is supported on two Teflon®-bushing bearings where rubbing occurs. The rotor's mass center is roughly centered between the bearings. The rotor is contained in a boom-mounted housing. The *RCl* was approximately 30 at the two contacts, which is small for a turbomachine; e.g., the rub contact location in Bartha's test rig has *RCl* close to 500. Also, the running speed ω can be low, ranging from 26 rpm for a wind speed of 1m/sec to 3800 rpm for 96m/sec. The combination of small *RCl*, low running speed, relatively high Coulomb friction at the rub interface, plus other (proprietary) factors produced the whirl-whip possibility. The Coulomb friction increased with operation time as Teflon® was transferred from the bushing to the shaft. NRG's experience is the first reported case of dry friction whip and whirl with rubbing at two contact locations.

The present paper presents a new rotor-stator model with rubbing at two contact location. Assuming that the same *RCl* holds for both contacts, the following two analytical solutions may be developed: (1) Mode 1. The precessing contact forces at both locations are in phase. (2) Mode 2. The precessing reaction contact forces at the two locations are 180° out of phase. The solution approach basically follows Black [2], producing *U*-shaped curves for the level of Coulomb friction that is required to produce whirling contact. These two response modes were cited by Kärkkäinen et al. [13] for motion of a rotor supported by magnetic bearings that drops on to the retainer bearing. A nonlinear, time-transient model will also be used to investigate the analytical solutions plus producing solutions for cases in which the *RCl* ratios are different at the two rubbing-contact locations.

NOMENCLATURE

A	$\boldsymbol{Z_{sL}Z_{sR}} - (J_{s12}\Omega^2)^2$
C_{rL}, C_{rR}	Clearance at rub surface [L]
D_w	$\boldsymbol{W_{11}W_{22}\text{-}W^2}$
$N_{L,}\ N_R$	Normal reaction on rotor at two contacts [F]
a	Imbalance displacement amplitude [L]
$c_{sL,}\ c_{rL}$	Stator support Damping constants [F t/L]
$f_{fL,}\ f_{fR}$	Friction force on rotor at two contacts [F]
$f_L\ f_R$	Reaction forces in complex form [F]
$f_{rLX}, f_{rRX}, f_{rLY}$ f_{rRY}	Reaction forces on the rotor at 2 contacts in the 2 planes [F]
$K_{sL,}\ K_{rL,}$	Stiffness constants [F/L]
l	Length of rotor between contact location [L]
l_g	Position of rotor center of mass from origin illustrated in Figure 1(a) with respect to reference frame fixed to ground [L]
l_s	Length of stator [L]
l_{sg}	Position of center of mass of stator with respect to origin illustrated in Figure 3(a) with respect to reference frame fixed to ground [L]
m_s, m_r	Mass of stator/rotor [M]
$rrL,\ rrR$	Rotor coordinates in complex form [L]
$r_{rLX,}\ r_{rRX},$ $r_{rLY},\ r_{rRY}$	Rotor coordinates at the 2 contacts in the 2 planes [L]
$rsLX, rsRX,$ $rsLY,\ rsRY$	Stator coordinates at the 2 contacts in the 2 planes [L]
$rsR\ rsR$	Stator coordinates in complex form [L]
rXc, rYc	Rotor coordinates of center of gravity [L]
Ω	Backward precessional angular velocity [1/t]
ω	Rotor angular velocity [1/t]
ω_{ns}	Stator natural frequency [1/t]
ω_{nc}	Combined rotor stator natural frequency [1/t]
θ_{rY}, θ_{rX}	The rotor's inclination with respect to the horizontal and vertical axes [-]

γ	Phase introduced in Eq. (10) [-]
μ	Coefficient Of friction

Subscripts

L	Left contact
R	Right contact
r	Rotor
s	Stator

Acronyms

BP	Backward Precessional
RCl	Radius to Clearance Ration

TWO-POINT RUBBING CONTACT MODEL FOR A RIGID ROTOR SUPPORTED BY AN ELASTICALLY SUPPORTED RIGID STATOR

This analysis applies for rubbing contact at two locations between a rigid-body rotor and a rigid-body stator that is supported by springs and dampers. The rotor has 5 degrees of freedom (axial motion is not allowed). The stator has four degrees of freedom; two displacements plus pitch and yaw. Rubbing contact can occur between the rotor and stator at two different locations. Gravity is neglected.

Rotor Equations of Motion

Figure 1(a) illustrates a rigid rotor temporarily located in the *X-Z* plane. It can contact at two locations with a rigid-body stator (shown below). The left and right contact locations are identified, respectively, by subscripts *L* and *R*. The distance between contact locations is *l*. The vectors $\boldsymbol{r_{rL}}, \boldsymbol{r_{rR}}$ locate the rotor's axis at the left and right contact locations, respectively. The rotor's mass center lies in a plane perpendicular to the rotor's geometric axis and is located the axial distance l_g from the left contact location. Figure 1(b) shows the mass center position within a plane perpendicular to the Z axis located by $\boldsymbol{r_g} = \boldsymbol{I}r_{gX} + \boldsymbol{J}r_{gY}$. The rotor is rotating in the counter clockwise direction with constant angular velocity ω. Its geometric center is located in this plane by $\boldsymbol{r_c} = \boldsymbol{I}r_{cX} + \boldsymbol{J}r_{cY}$. The rotor's mass center is displaced the distance *a* from its geometric axis, and is located in the *X-Y* system by:

$$r_{gX} = r_{cX} + a\cos\omega t \;,\; r_{gY} = r_{cY} + a\sin\omega t \tag{1}$$

The rotor's inclination with respect to the horizontal *X-Z* plane is defined by the (small) angle θ_{rY} . In the *X-Z* plane, the rotor's left and right positions at the contact with the stator are defined, respectively, by the displacement vectors $\boldsymbol{r_{rLX}}, \boldsymbol{r_{rRX}}$.

The coordinates are related by:

$$\theta_{rY} = \frac{(r_{rRX} - r_{rLX})}{l},\; r_{Xc} = r_{rLX} + \theta_{rY} l_g = r_{rRX}\frac{l_g}{l} + r_{rLX}(1 - \frac{l_g}{l})$$

In the *Y-Z* plane, the corresponding results are:

$$\theta_{rY} = \frac{(r_{rRX} - r_{rLX})}{l},\; r_{Xc} = r_{rLX} + \theta_{rY} l_g = r_{rRX}\frac{l_g}{l} + r_{rLX}(1 - \frac{l_g}{l})$$

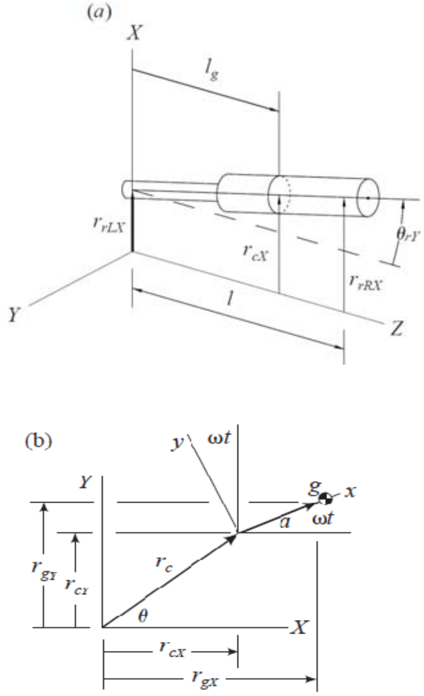

Figure 1. (a) Rotor in *X-Z* plane, (b) Transverse plane through rotor mass center

The governing equations of motion will be developed using Lagrange's equations. The rotor's kinetic energy is :

$$\begin{aligned} T &= (\frac{m_r}{2}\dot{r}_{gX}^2 + \frac{I_{rg}}{2}\dot{\theta}_{rY}^2) + (\frac{m_r}{2}\dot{r}_{gY}^2 + \frac{I_{rg}}{2}\dot{\theta}_{rX}^2) \\ &= \frac{m_r}{2}[-a\omega\sin\omega t + \dot{r}_{rRX}\frac{l_g}{l} + \dot{r}_{rLX}(1 - \frac{l_g}{l})]^2 + \frac{I_{rg}}{2}[\frac{(\dot{r}_{rRX} - \dot{r}_{rLX})}{l}]^2 \\ &+ \frac{m_r}{2}[a\omega\cos\omega t + \dot{r}_{rRY}\frac{l_g}{l} + \dot{r}_{rLY}(1 - \frac{l_g}{l})]^2 + \frac{I_{rg}}{2}[\frac{(\dot{r}_{rLY} - \dot{r}_{rRY})}{l}]^2 \end{aligned}$$

Neglecting gravity, there is no potential energy, and Lagrange's equations of motion in the *X-Z* plane are

$$\begin{bmatrix} m_r(1 - \frac{l_g}{l})^2 + \frac{I_g}{l^2} & m_r\frac{l_g}{l}(1 - \frac{l_g}{l}) + \frac{I_g}{l^2} \\ m_r\frac{l_g}{l}(1 - \frac{l_g}{l}) + \frac{I_g}{l^2} & m_r(\frac{l_g}{l})^2 + \frac{I_g}{l^2} \end{bmatrix} \begin{Bmatrix} \ddot{r}_{rLX} \\ \ddot{r}_{rRX} \end{Bmatrix} \tag{2}$$

(2)

$$= \begin{Bmatrix} f_{LX} + ma\omega^2\cos\omega t(1 - \frac{l_g}{l}) \\ f_{RX} + ma\omega^2\cos\omega t(\frac{l_g}{l}) \end{Bmatrix},$$

and in the *Y-Z* plane are

$$\begin{bmatrix} m_r(1-\frac{l_g}{l})^2+\frac{I_g}{l^2} & m_r\frac{l_g}{l}(1-\frac{l_g}{l})+\frac{I_g}{l^2} \\ m_r\frac{l_g}{l}(1-\frac{l_g}{l})+\frac{I_g}{l^2} & m_r(\frac{l_g}{l})^2+\frac{I_g}{l^2} \end{bmatrix}\begin{Bmatrix} \ddot{r}_{rYL} \\ \ddot{r}_{rYR} \end{Bmatrix} = \begin{Bmatrix} f_{YL}+ma\omega^2\cos\omega t(1-\frac{l_g}{l}) \\ f_{YR}+ma\omega^2\cos\omega t(\frac{l_g}{l}) \end{Bmatrix}, \tag{3}$$

where f_{LX}, f_{LY} and f_{RX}, f_{RY} are the reaction-force components acting on the rotor at the left and right hand contact points, respectively. In condensed form, Eqs.(2-3) can be combined as the single complex matrix equation.

$$\begin{bmatrix} J_{r11} & J_r \\ J_r & J_{r22} \end{bmatrix}\begin{Bmatrix} \ddot{\boldsymbol{r}}_{\boldsymbol{rL}} \\ \ddot{\boldsymbol{r}}_{\boldsymbol{rR}} \end{Bmatrix} = \begin{Bmatrix} \boldsymbol{f_L} \\ \boldsymbol{f_R} \end{Bmatrix} + ma\omega^2 e^{j\omega t}\begin{Bmatrix} (1-\frac{l_g}{l}) \\ (\frac{l_g}{l}) \end{Bmatrix}, \tag{4}$$

where

$$J_{r11}=[m_r(1-\frac{l_g}{l})^2+\frac{I_{rg}}{l^2}],\ J_{r22}=[m_r(\frac{l_g}{l})^2+\frac{I_{rg}}{l^2}],$$
$$J_r=[m_r\frac{l_g}{l}(1-\frac{l_g}{l})+\frac{I_{rg}}{l^2}] \tag{5}$$

$$\boldsymbol{r_{rL}} = r_{rXL}+\boldsymbol{j}r_{rYL},\ \boldsymbol{r_{rR}} = r_{rXR}+\boldsymbol{j}r_{rYR},$$
$$\boldsymbol{f_L} = f_{XL}+\boldsymbol{j}r_{YL},\ \boldsymbol{f_R} = f_{XR}+\boldsymbol{j}r_{YR} \tag{6}$$

Stator Equations of Motion

Figure 3 illustrates the rotor and stator axial positions. As shown, the rotor is centered within the clearances. The radial clearances at the left and right contact locations are, respectively, C_{rR}, C_{rL}. The corresponding rotor radii at the contact locations are r_{rR}, r_{rL}. The stator can move up and down plus pitch and yaw. From Figure 2, θ_{sY} and r_{sCX} are defined by

$$\theta_{sY}=\frac{(r_{sRX}-r_{sLX})}{l},\ r_{sgX}=r_{sLX}+\theta_{sY}l_g=r_{sRX}\frac{l_g}{l}+r_{sLX}(1-\frac{l_g}{l})$$

In the *Y-Z* plane, the corresponding results are:

$$\theta_{sX}=\frac{(r_{sYL}-r_{sYR})}{l},\ r_{sgY}=r_{sYL}+\theta_{sX}l_g=r_{sYR}\frac{l_g}{l}+r_{sYL}(1-\frac{l_g}{l})$$

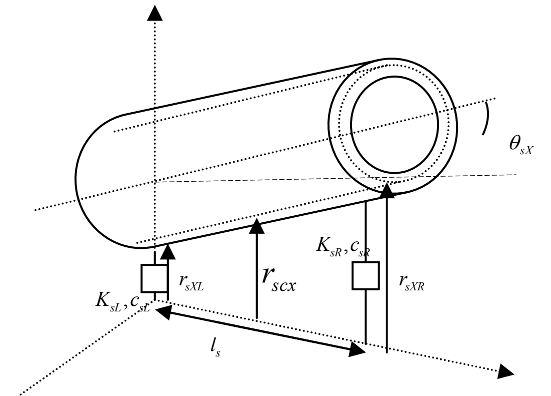

Figure 2. Stator Coordinates showing support connections in the X-Z plane

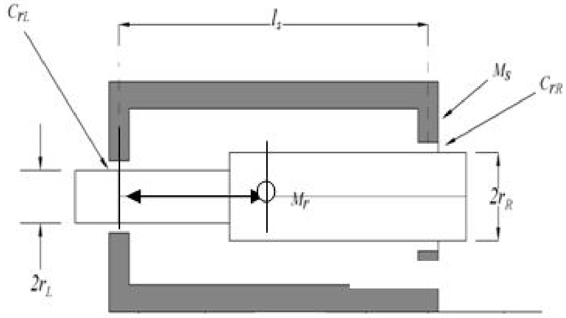

Figure 3. Section View Rotor and Stator Assembly Positions

Using Lagrange's equations, the stator's matrix equations of motion (in complex form) are

$$\begin{bmatrix} J_{s11} & J_s \\ J_s & J_{s22} \end{bmatrix}\begin{Bmatrix} \ddot{\boldsymbol{r}}_{\boldsymbol{sL}} \\ \ddot{\boldsymbol{r}}_{\boldsymbol{sR}} \end{Bmatrix} + \begin{bmatrix} c_{sL} & 0 \\ 0 & c_{sR} \end{bmatrix}\begin{Bmatrix} \dot{\boldsymbol{r}}_{\boldsymbol{sL}} \\ \dot{\boldsymbol{r}}_{\boldsymbol{sR}} \end{Bmatrix} + \begin{bmatrix} K_{sL} & 0 \\ 0 & K_{sR} \end{bmatrix}\begin{Bmatrix} \boldsymbol{r_{sL}} \\ \boldsymbol{r_{sR}} \end{Bmatrix} = -\begin{Bmatrix} \boldsymbol{f_L} \\ \boldsymbol{f_R} \end{Bmatrix} \tag{7}$$

Where

$$J_{s11}=[m_s(1-\frac{l_{sg}}{l_s})^2+\frac{I_{sg}}{l_s^2}],\ J_{s22}=[m_s(\frac{l_{sg}}{l_s})^2+\frac{I_{sg}}{l_s^2}],$$
$$J_s=[m_s\frac{l_g}{l_s}(1-\frac{l_g}{l_s})+\frac{I_{sg}}{l_s^2}],$$

and

$$\boldsymbol{r_{sL}} = r_{sXL}+\boldsymbol{j}r_{sYL},\ \boldsymbol{r_{sR}} = r_{sXR}+\boldsymbol{j}r_{sYR} \tag{8}$$

Constraint Equations

Figure 4 illustrates the contact reaction forces and geometry relations between the rotor and stator displacement vectors at either contact location. From this figure, the constraint equations at the left and right contact points are

$$C_{rR}e^{j\gamma_r} = \boldsymbol{r_{rR}} - \boldsymbol{r_{sR}}\ ,\ C_{rL}e^{j\gamma_l} = \boldsymbol{r_{rL}} - \boldsymbol{r_{sL}} \qquad (9)$$

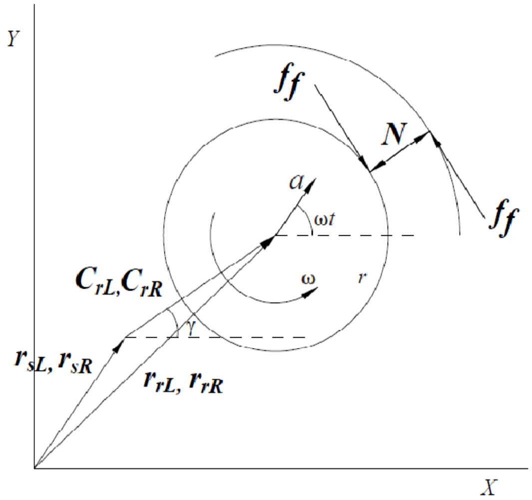

Figure 4. Clearance Diagram (Constraints)

Two-Contact Model Natural Frequencies and Configurations

Crandall used a Föppl-Jeffcott rotor model with two degrees of freedom plus a particle model for the stator with two degrees of freedom. Accordingly, the rotor had a natural frequency ω_{nr}; the stator had a natural frequency ω_{ns} . Pinning the rotor and stator together at the contact point produced the pinned natural frequency ω_{nc}. For the present model, the unsupported rotor can move radially (bounce) and rotate about its mass center (pitch or yaw), and has a zero natural frequency associated with both displacement and rotation.

We will consider the three rotor configurations shown in figure 5 with a disk that is centered, offset to a ¾ location, and overhung. The axisymmetric stator has two degrees of freedom in the plane of the paper. For the models considered here, the support bearing stiffness coefficients are equal, and located equidistant from the stator's mass center. Hence, the stator has uncoupled "bounce" (displacement only) and "pitch" (rotation only) modes. Pinning the rotor and stator together at the contact locations will produce two modes in the plane of the paper. Except for the centered mass location, the pinned modes will include displacement and rotation coupling. None the less, we will refer to the pinned modes as "bounce" and "pitch".

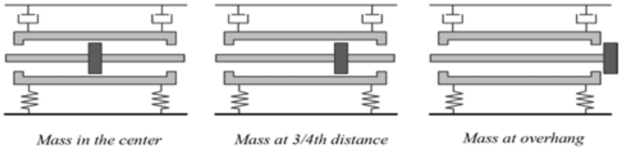

Figure 5. Mass locations considered

MODE 1 SOLUTION DEVELOPMENT

A planar precessing mode is assumed with the normal reaction contact forces $\boldsymbol{N_L}, \boldsymbol{N_R}$ in phase at the two contact points; hence, $\gamma_l = \gamma_R = \gamma$. Note: This equation does not require that the *motion* be in phase at the contact points; i.e., $\boldsymbol{r_{rL}}$ and $\boldsymbol{r_{rR}}$ are not necessarily in phase. The contact force components at the contact points are

$$\begin{gathered} f_{rLX} = -N_L \cos\gamma + f_{fL}\sin\gamma\ ,\ f_{rLY} = -N_L\sin\gamma - f_{fL}\cos\gamma \\ f_{rRX} = -N_R\cos\gamma + f_{fR}\sin\gamma\ ,\ f_{rRY} = -N_R\sin\gamma - f_{fR}\cos\gamma \end{gathered} \qquad (10)$$

In complex form, they become,

$$\begin{gathered} \boldsymbol{f_L} = -N_L(\cos\gamma + \boldsymbol{j}\sin\gamma) + f_{fL}(\cos\gamma - \boldsymbol{j}\sin\gamma) \\ = -(N_L + \boldsymbol{j}f_{fL})e^{j\gamma}\ \boldsymbol{;}\ \ \boldsymbol{f_R} = -(N_R + \boldsymbol{j}f_{fR})e^{j\gamma} \end{gathered} \qquad (11)$$

Substituting from Eq.(11) into Eq.(4) and neglecting imbalance, the rotor's matrix equation of motion is :

$$\begin{bmatrix} J_{r11} & J_r \\ J_r & J_{r22} \end{bmatrix} \begin{Bmatrix} \boldsymbol{\ddot{r}_{rL}} \\ \boldsymbol{\ddot{r}_{rR}} \end{Bmatrix} = -\begin{Bmatrix} (N_L + \boldsymbol{j}f_{fL}) \\ (N_R + \boldsymbol{j}f_{fR}) \end{Bmatrix} e^{j\gamma}$$

Solving for the accelerations nets:

$$\begin{aligned} \boldsymbol{\ddot{r}_{rL}} &= -\frac{l^2}{I_{rg}m_r}[J_{r22}(N_L + \boldsymbol{j}f_{fL}) - J_r(N_R + \boldsymbol{j}f_{fR})]e^{j\gamma} \\ \boldsymbol{\ddot{r}_{rR}} &= -\frac{l^2}{I_{rg}m_r}[J_{r11}(N_R + \boldsymbol{j}f_{fR}) - J_r(N_L + \boldsymbol{j}f_{fL})]e^{j\gamma} \end{aligned} \qquad (12)$$

The stator equations of motion, Eq.(7) become:

$$\begin{bmatrix} J_{s11} & J_s \\ J_s & J_{s22} \end{bmatrix} \begin{Bmatrix} \boldsymbol{\ddot{r}_{rL}} \\ \boldsymbol{\ddot{r}_{rR}} \end{Bmatrix} + \begin{bmatrix} c_{sL} & 0 \\ 0 & c_{sR} \end{bmatrix} \begin{Bmatrix} \boldsymbol{\dot{r}_{rL}} \\ \boldsymbol{\dot{r}_{rR}} \end{Bmatrix} + \begin{bmatrix} K_{sL} & 0 \\ 0 & K_{sR} \end{bmatrix} \begin{Bmatrix} \boldsymbol{r_{rL}} \\ \boldsymbol{r_{rR}} \end{Bmatrix} = \begin{Bmatrix} (N_L + \boldsymbol{j}f_{fL}) \\ (N_R + \boldsymbol{j}f_{fR}) \end{Bmatrix} e^{j\gamma} \qquad (13)$$

Substituting the assumed solutions,

$$\begin{aligned} \boldsymbol{r_{sL}} &= \boldsymbol{r_{sL0}}e^{j(\gamma - \Omega t)} & \boldsymbol{r_{rL}} &= \boldsymbol{r_{rL0}}e^{j(\gamma - \Omega t)} \\ \boldsymbol{r_{sR}} &= \boldsymbol{r_{sR0}}e^{j(\gamma - \Omega t)} & \boldsymbol{r_{rR}} &= \boldsymbol{r_{rR0}}e^{j(\gamma - \Omega t)}, \end{aligned} \qquad (14)$$

with precession in the clockwise direction at the rate Ω (opposite to the shaft rotation direction ω) into Eqs.(12-13) produces:

$$\boldsymbol{r_{rR0}} = \frac{l^2}{I_{rg} m_r \Omega^2}[J_{r11}(N_R + \boldsymbol{j} f_{fR}) - J_r(N_L + \boldsymbol{j} f_{fL})]$$
$$\boldsymbol{r_{rL0}} = \frac{l^2}{I_{rg} m_r \Omega^2}[J_{r22}(N_L + \boldsymbol{j} f_{fL}) - J_r(N_R + \boldsymbol{j} f_{fR})]$$
$$\boldsymbol{r_{sL0}} = \frac{(N_L + \boldsymbol{j} f_{fL}) Z_{sR} + J_s \Omega^2 (N_R + \boldsymbol{j} f_{fR})}{\boldsymbol{A}} \quad (15)$$
$$\boldsymbol{r_{sR0}} = \frac{(N_R + \boldsymbol{j} f_{fR}) Z_{sL} + J_s \Omega^2 (N_L + \boldsymbol{j} f_{fL})}{\boldsymbol{A}}$$

where

$$\boldsymbol{A} = \boldsymbol{Z_{sL}} \boldsymbol{Z_{sR}} - (J_{s12}\Omega^2)^2, \; \boldsymbol{Z_{sL}} = (k_{sL} - J_{s11}\Omega^2) - \boldsymbol{j}\Omega c_{sL}, \quad (16)$$
$$\boldsymbol{Z_{sR}} = (k_{sR} - J_{s22}\Omega^2) - \boldsymbol{j}\Omega c_{sR}$$

Similarly, the constraint Eq.(9) becomes

$$\boldsymbol{C_{rR}} = \boldsymbol{r_{rR0}} - \boldsymbol{r_{sR0}}, \boldsymbol{C_{rL}} = \boldsymbol{r_{rL0}} - \boldsymbol{r_{sL0}} \quad (17)$$

Substituting $\boldsymbol{r_{rL0}}, \boldsymbol{r_{rR0}}, \boldsymbol{r_{sL0}}, \boldsymbol{r_{sR0}}$ from Eq.(15) into Eq.(17) gives

$$C_{rL} = (N_L + \boldsymbol{j} f_{fL})[\frac{J_{r22} l^2}{I_g m_r \Omega^2} - \frac{\boldsymbol{Z_{sR}}}{\boldsymbol{A}}] - (N_R + \boldsymbol{j} f_{fR})[\frac{J_r l^2}{I_g m_r \Omega^2} + \frac{J_s \Omega^2}{\boldsymbol{A}}]$$
$$C_{rR} = -(N_L + \boldsymbol{j} f_{fL})[\frac{J_r l^2}{I_g m_r \Omega^2} + \frac{J_s \Omega^2}{\boldsymbol{A}}] + (N_R + \boldsymbol{j} f_{fR})[\frac{J_{r11} l^2}{I_g m_r \Omega^2} - \frac{\boldsymbol{Z_{sL}}}{\boldsymbol{A}}]$$

Restating Eq.(18) gives

$$\begin{bmatrix} \boldsymbol{W_{11}} & \boldsymbol{-W} \\ \boldsymbol{-W} & \boldsymbol{W_{22}} \end{bmatrix} \begin{bmatrix} N_L + \boldsymbol{j} f_{fL} \\ N_R + \boldsymbol{j} f_{fR} \end{bmatrix} = \begin{bmatrix} C_{rL} \\ C_{rR} \end{bmatrix}, \quad (19)$$

where

$$\boldsymbol{W_{11}} = [\frac{J_{r22} l^2}{I_g m_r \Omega^2} - \frac{\boldsymbol{Z_{sR}}}{\boldsymbol{A}}], \; \boldsymbol{W} = [\frac{J_r l^2}{I_g m_r \Omega^2} + \frac{J_s \Omega^2}{\boldsymbol{A}}],$$
$$\boldsymbol{W_{22}} = [\frac{J_{r11} l^2}{I_g m_r \Omega^2} - \frac{\boldsymbol{Z_{sL}}}{\boldsymbol{A}}]$$

Eq.(19)'s solution is

$$(N_L + \boldsymbol{j} f_{fL}) = \frac{C_{rL}\boldsymbol{W_{22}} + C_{rR}\boldsymbol{W}}{\boldsymbol{D_W}}$$
$$(N_R + \boldsymbol{j} f_{fR}) = \frac{C_{rR}\boldsymbol{W_{11}} + C_{rL}\boldsymbol{W}}{\boldsymbol{D_W}}, \quad (20)$$

where

$$\boldsymbol{D_W} = \boldsymbol{W_{11}} \boldsymbol{W_{22}} - \boldsymbol{W}^2$$

Evaluating the reaction forces in Eq.(19) will produce the normal reaction magnitudes N_L, N_R and friction-restraint force magnitudes f_{fL}, f_{fR}, netting the required Coulomb-friction factors:

$$\mu_{Lrequired}(\Omega) = \frac{f_{fL}}{N_L}, \; \mu_{Rrequired}(\Omega) = \frac{f_{fR}}{N_R} \quad (21)$$

Contact between the rotor and stator at the left and right locations requires

$$N_L(\Omega) > 0, \; N_R(\Omega) > 0 \quad (22)$$

Note that contact is possible at one location while absent at the other, for example $N_L > 0, N_R = 0$.

With contact at both locations, slipping can occur at one of the two contact surfaces with rolling-without slipping at the other. However, rolling without slipping *for both locations* requires

$$0 \le \mu_{Lrequired} \le \mu_L, \; 0 \le \mu_{Rrequired} \le \mu_R \quad (23)$$

where μ_L, μ_R are the available static Coulomb damping coefficients at the left and right contact locations.

(18)

For Black and Crandall's single-contact models, contact could not be maintained $(N \le 0)$ for $0 < \Omega < \omega_{nr}$, becoming possible for $\omega_{nr} < \Omega < \omega_{nc}$. Within this precession-frequency band, rolling without slipping was predicted for $0 \le \mu_{required} \le \mu$, yielding Black's 'U-shaped', $\mu_{required}$ versus Ω curves. For rolling without slipping, the running speed ω and precessional frequency Ω are related by $\Omega = (r / C_r)\omega$ producing a 'tracking' super synchronous response. Whipping initiated for $\Omega = \omega_{nc}$ with a super synchronous response fixed at ω_{nc} for increasing speed ω. For $\Omega > \omega_{ns}$, whirling motion was again possible.

MODE 1 ANALYTIC EXAMPLE SOLUTIONS

The following numerical values are used for prediction of whip and whirl characteristics for the two-point-contact model. They represent no specific piece of machinery.

$$l = .29\ m,\ l_s = .27\ m, C_{rR} = C_{rL} = 3.81E-04 \text{ m}$$
$$r_{rL} = r_{rR} = 3.81\text{E}-02\text{m}, I_g = .029\ kgm^2, \; I_{sg} = .206\ kgm^2$$
$$m_s = 21.44\ kg, \; m_r = 9.99\ kg, \; \mu = .5 \quad (24)$$

The support stiffness and damping used at the stator's ends are:

$$K_{sL} = K_{sR} = 4.7E+6 \text{ N/m}; \; c_{sL} = c_{sR} = 324.9 \text{ N-s/m} \quad (25)$$

Mode 1. Rotor Disk Centered

The undamped stator and lowest rotor-stator pinned natural frequencies are:

$$\begin{aligned}&\omega_{ns}(bounce) = 105.3\text{Hz},\ \omega_{ns}(pitch) = 144.9\text{Hz}\\&\omega_{nc1}(bounce) = 87.03\text{Hz},\ \omega_{nc}(pitch) = 135.5\text{Hz}\end{aligned} \qquad (26)$$

Figure 6 follows from Eq.(20) with the data of Eqs.(24-25), and shows the static Coulomb coefficient required (μ_{req}) to prevent slipping as a function of the precession frequency Ω . If μ_{req} is positive and less than the available (μ_{avail}) Coulomb friction, whirl is possible. Figure 6 shows this same outcome with whirling occurring between zero (the rotor's natural frequency) and the first combined rotor-stator bounce natural frequency 87.3 Hz and above the stator bounce natural frequency 105 Hz. Whip occurs between these limiting whirl frequencies. For μ_{avail}=0.5, whirl can occur for precession frequencies up to 84.5Hz (point *A*) and beyond 109.4 Hz (point *B*). Whip is expected between points *A* and *B*.

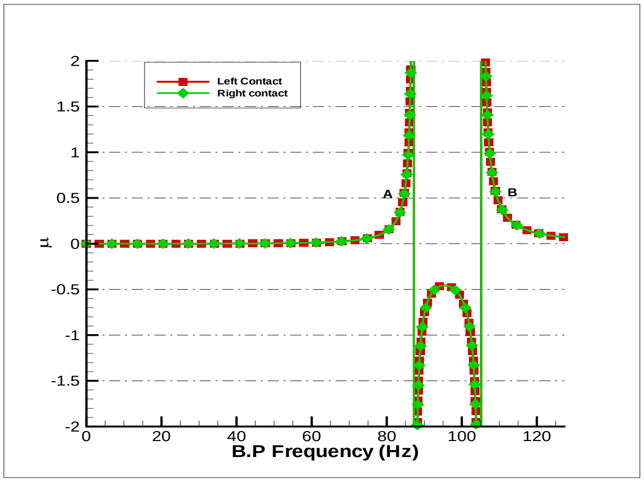

Figure 6. Mode 1, *RCl* L= *RCl* R , Disk at Center

Mode 1. Rotor Disk at ¾ location

Moving the disk does not change the stator natural frequency but changes the rotor center of gravity, thus changing the value of l_g (rotor center of gravity location) from .145m to .22m and value of I_g (moment of inertia) to .04kgm^2 from .02 kgm^2. The pinned rotor-stator natural frequencies are

$$\omega_{nc1}(bounce) = 87.03\text{Hz},\ \omega_{nc}(pitch) = 132.6\text{Hz} \qquad (27)$$

Figure 7 shows the whirl region extending from zero to the combined natural frequency corresponding of 87Hz. Whirling would be expected from zero to point *A* (83.66 Hz) where whipping would ensue until point *B*. Between *B* and *C* the right contact should whirl. However, once the required Coulomb friction for the left contact changes sign, whipping is expected, i.e., whipping motion at the left contact with whirling at the right location.

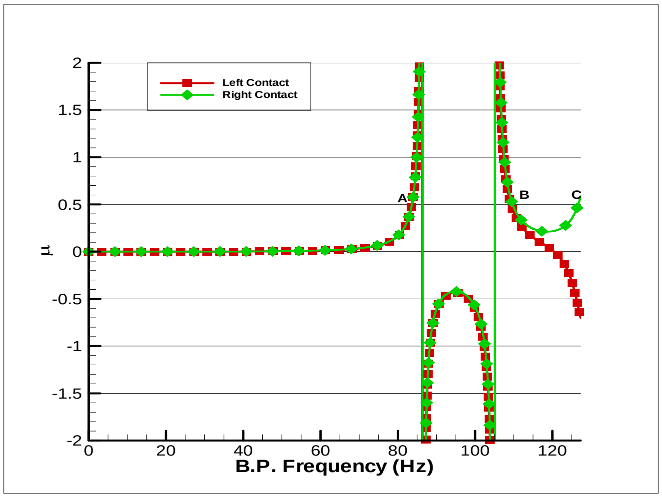

Figure 7 Disk at ¾ Location RCl$_L$= RCl$_R$. Mode 1

Mode 1. Rotor Disk at Overhung Location

The disk is shifted to a point beyond the right contact moving the C.G. to a position .26m from the left contact location and producing I_g=.07. For this location, the calculated values of pinned undamped natural frequencies are:

$$\omega_{nc1}(bounce) = 87.03\text{Hz},\ \omega_{nc2}(pitch) = 123\text{Hz} \qquad (28)$$

The mode-1 analytical solutions are not presented here because, as noted below, the nonlinear time-transient solutions are completely bear no resemblance to the analytical predictions.

MODE 2 ANALYTIC EXAMPLE SOLUTIONS

For this solution, we assume a planar precessing mode with *normal contact forces* 180° out of phase at the two contact locations; hence $\gamma_L = \gamma, \gamma_R = \gamma + \pi$. This stipulation does not produce *motion* that is out of phase at the two contact locations; i.e. $\boldsymbol{r}_{rL}$ and $\boldsymbol{r}_{rR}$ are not necessarily 180° out of phase. The same solution approach is used for this mode as for the Mode 1 solution and is detailed by Kumar [14]. Mode 2 solutions are presented by Kumar for all of the rotor configurations but are not given here because they could not be produced by the time-transient nonlinear model discussed below.

NONLINEAR SIMULATIONS

Introduction

Nonlinear time-transient simulations were carried out to: (1) Check on the analytical predictions for circumstances where they apply ($RCl_L = RCl_R$), and (2) Examine the nature of predicted solutions when these circumstances do not apply. The modeling approach used here was employed by Wilkes et al. and agreed very well with measurements. Hence, in the present study, the nonlinear predictions are assumed to correct in the conditions where the analytical solutions apply. An axisymmetric flexible-rotor/flexible-stator model was used, featuring component-mode synthesis to reduce problem dimensionality. The base code uses a Timoshenko beam finite elements model. Aside from rotor and stator flexibility, the structural dynamic model for the nonlinear model was the same as the rigid-body model of Eqs.(24-25). Details of the model are provided in Kumar [14].

Table 1 shows the cases that were simulated; however, space will permit a review of only a few of these. The *RCL* ratios of Table 1 are larger than Clark et al.'s [12] anemometer but smaller than values for many turbomachines which can range up to ~500.

Table 1 Division of Cases and Subcases for Simulation Model

Disk Position	Subcase	$\boldsymbol{RCL}_{\mathrm{L}}$	$\boldsymbol{RCL}_{\mathrm{R}}$
(A) center	(a)	100	100
	(b)	100	125
(B) ¾	(a)	100	100
	(b)	100	125
	(c)	125	100
(C) overhung	(a)	100	100
	(b)	100	125
	(c)	125	100

Table 2 Pinned Rotor-stator frequencies and damping factors

Disk Location	ω_{nb} (Hz)	Zeta_{nb}	ω_{np} (Hz)	Zeta_{np}	ω_{nbend} (Hz)	Zeta_{bend}
center	87.9	.019	133.8	.029	595.1	.009
¾	86.9	.019	127.9	.028	709.8	.013
Overhung	82.4	.018	115.4	.025	701.3	.005

Table 2 shows the damping ratio and damped natural frequency for the above three configurations. The pinned-rotor-stator values have been calculated using a very stiff connection defined by: ($K_{contact,L} = K_{contact,R}$ =4.5E+8 N/m, $c_{contact,L} = c_{contact,R}$ =2.1E+4 N-s/m) at the contact locations.

For the support stiffness values of Eq.(25) the stator mode shapes are from highest to lowest, a nominally rigid bounce mode, a nominally rigid pitch mode, and a bending mode. For the damping values of Eq.(25), the stator damped natural frequencies and damping factors are:

$$\omega_{ns1} = 105.4Hz,\ \zeta_{s2} = .023;\ \omega_{ns2} = 143Hz,\ \zeta_{s1} = .031;$$
$$\omega_{ns3} = 8233Hz,\ \zeta_{s3} = 0.000; \qquad (29)$$

Contact Reaction Force Model

Hunt and Crossley [11] defined the following nonlinear interaction-force model at a rub location

$$N = k_{nl,1}\delta + k_{nl,2}\delta^2 + c_{nl,1}\dot{\delta} + c_{nl,2}\dot{\delta}\delta \qquad (30)$$

where $k_{nl,1}$, $k_{nl,2}$ and $c_{nl,1}$ are stiffness and damping coefficients and δ represents the deflection at the rub surface. For the current work, a linear model was used with the following stiffness and damping values:

$$k_{n1,1L} = k_{n1,1R} = 1.75E+11 \text{ N/m};\ k_{n1,2L} = k_{n1,2R} = 0 = c_{n1,2L} = c_{n1,2R} = 0$$
$$c_{n1,1L} = c_{n1,1R} = 1.75E+05 \text{ N-s/m} \qquad (31)$$

These contact stiffness and damping coefficient values were obtained by scaling values from Wilkes [16] and further adjusting them to get better responses and results.

The transverse contact reaction force due to friction is :

$$F_f = \mu N \operatorname{sgn}(V_t) \qquad (32)$$

where $\operatorname{sgn}(V_t)$ accounts for relative transverse contact velocity and $\boldsymbol{V_t}$ is the relative tangential surface velocity at contact given by :

$$\boldsymbol{V_t} = \dot{r}_{rX}\boldsymbol{I} + \dot{r}_{rY}\boldsymbol{J} + \boldsymbol{\omega}\times\boldsymbol{r} \qquad (33)$$

The rotor radii at the contact are: r_{rL}= r_{rR} =38.1mm. The available coefficient of friction was taken to be μ =.5 to improve the chances of exhibiting whip and whirl behavior.

Imbalance

The following API imbalance was added at the disk

$$imbalance(\text{oz-inch}) = \frac{4 * w(lbs)}{N(rpm)} \qquad (34)$$

For ω = 6000 rpm, the imbalance is 3.43 gm-cm, and this imbalance was introduced in the CASE A; (a) and did not make any substantial changes to the results.

Simulation Procedures

Gravity is neglected, and the rotor and stator initial conditions were initially set to zero. Whip and whirl behavior was initiated by exciting the shaft with an impulsive force thereby bringing the rotor in contact with the stator. Each rotor-speed simulation was run for 1.5 seconds (real time) to obtain a frequency resolution of .67Hz. The Runge Kutta algorithm produced multiple predictions for the contact velocity across each time step, and an average of these valued was used. A (small) viscous damper connected the rotor to the stator at the disk location to attenuate the shock created by the initial rotor-stator contact. Its damping coefficient was *c= 52* N-s/m.

For speed-increasing studies, the initial simulation was run at 20 rpm until a steady-state cycle persisted, followed by running a new simulation with increased rotor speed from the previous state, etc. The procedure was repeated for increasing rotor speed from 20 to 258rpm. The predictions, recorded for each simulation consisted of the rotor's position and velocity at each of the contact points relative to the stator's position. An FFT was used to convert these time histories into frequency-domain results. Relative contact point-velocities were analyzed to determine the presence of either pure sliding or rolling with slipping.

A similar procedure was used for analyzing the whip and whirl behavior when speeds are decreased. The motion is initiated by exciting the shaft with an impulsive force thereby bringing the rotor in contact with the stator at 252 rpm. This simulation was run until a steady state persisted, followed by running a new simulation with decreased rotor speed from the previous state (no excitation). The procedure was repeated for decreasing rotor speed from 252 rpm to 20 rpm.

Comparison between Analytical and Numerical Predictions

Direct comparison between analytical and simulation predcitions is difficult because the analytical solutions predict required μ values versus backward precession (*BP*) frequencies, while simulations produce predictions of forward and backward precession frequencies versus ω. If the simulations predict that a *BP* increases with increasing ω, a whirl regime is assumed to apply. If the *BP* frequency remains constant with increasing ω, a whipping regime is presumed to occur.

NONLINEAR SIMULATION PREDICTIONS

Disk at Center, $RCl_L = RCl_R = 100$

Figure 7(a) shows a two sided FFT waterfall plot (left contact, *X* motion) for speed increasing. The whirl frequencies are dominant in the negative frequency region showing backward precession. Harmonic sidebands are present during the whip regions due to the presence of partial rub and contact loss at the contact surfaces.

Figure 7(b) illustrates the main predicted *BP* frequency versus ω for speed increasing and speed decreasing at the left contact location. For speed increasing, the whirl region extends to ω=56rpm (*BP* frequency increasing with increasing rotor speed) when whipping initiates at *BP*=84.6Hz. Whipping extends to ω=160rpm beyond which it again jumps to whirl. The analytical predictions of Figure 6 show a very similar behavior for the jump from whirl to whip with a whip frequency of 84.5Hz.

For decreasing rotor speed, the rotor stays in whirl longer before jumping to the whipping mode at approximately 70 rpm, which does not agree with Figure 6. The same whip frequency of *BP*=84.6Hz is obtained for run up and run down plus the same whip-to-whirl shift at ω =56 rpm. Similar differing test characteristics in run up and run down were reported in Wilkes et al. [10] test results. In 2010, Jiang et al. [17] analytically predict this sort of multi-valued solution behavior stating that the contact stiffness is required in their analytical model to obtain a multi-valued solution. Contact stiffness is also present in these nonlinear simulation but was not used in obtaining Figure 6.

The V_{tL} versus ω predictions of Figure 7(c) for speed increasing agree with the comparable speed-increasing results of Figure 7(b). For the initial whirling range up to 56 rpm, the contact velocity stays at zero (rolling without slipping), followed by a continuous increase in contact velocity until it enters the second whirl region at 160 rpm, and the contact velocity goes back to zero. Although not illustrated, the right contact velocity shows the same behavior.

These are all Mode-1 solutions and were obtained by impulsive excitation at the rotor’s center. Attempts were made to excite Mode-2 solutions by:

(1) Hitting the ends with impulses in opposite directions

(2) Providing an impulsive moment at the center

Neither approach produced the Mode-2 motion predicted in Figure 9. The disturbed motion would eventually become Mode 1 and give the same results as above.

Disk at ¾ Location; RCl_L=100, RCl_R=125

Figure 8(a) characteristics are similar to Figure 7(b), showing whirl-like behavior at the left contact location for

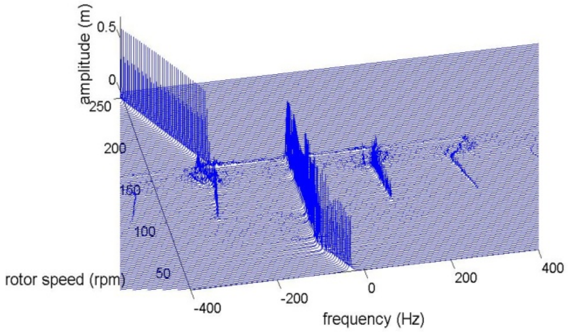

Figure 7.(a) 2-sided FFT Simulation Predictions for Left Contact

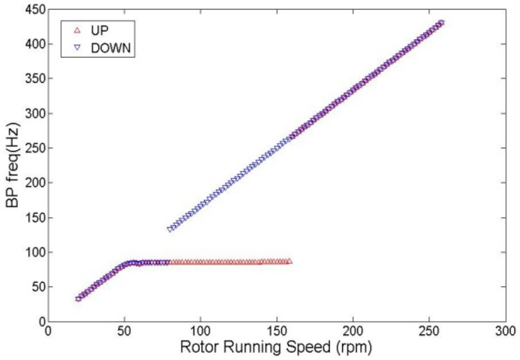

Figure. 7(b) Simulation Results for Left Contact

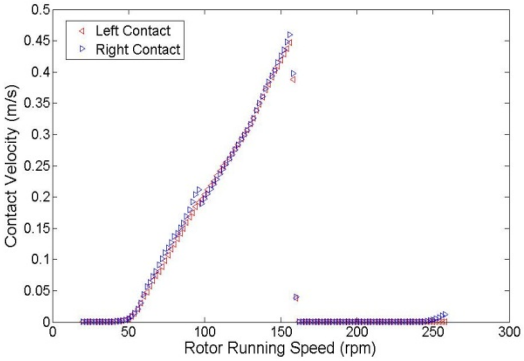

Figure. 7(c) Vt vs ω Speed Increasing

speeds up to ~50 rpm followed by whip with *BP*=84.6 Hz, followed by a higher-speed region of whirl-like behavior. As with the predictions in Figure 7(b), the predicted running speeds of the higher-speed transition differ in the speed-increasing and speed-decreasing predictions.

In regard to the whirl-like regions, both contact points cannot experience rolling without slipping simultaneously since they have different *RCl* values. As shown in Figure 8(b), V_{tL} and V_{tR} are different and not zero within the whirl-like regimes of Figure 8(a). Generally, V_{tL} (*RCl*=100) is less than V_{tR} (*RCl*=125). The *BP* increases with increasing rotor speed "*mimicking"* whirl, while slipping continuously.

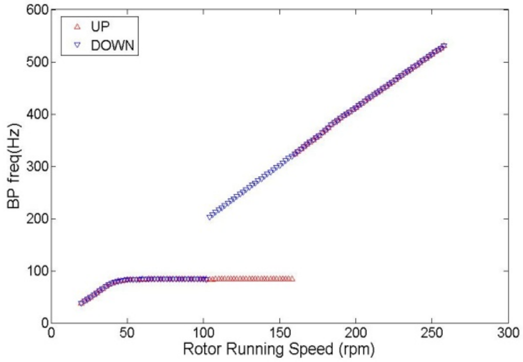

Figure. 8(a) Simulation Results for Left contact

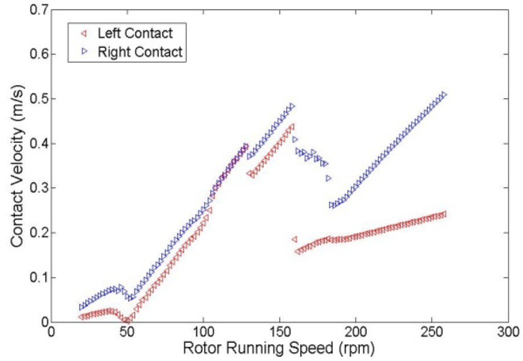

Figure. 8(b) Vt vs ω Speed Increasing

Disk at ¾ Location; RCl_L=125 RCl_R=100

In general, the plots for this configuration are similar to the RCl_L=100, RCl_R=125 predictions showing an initial "whirl-like" regime at lower speeds. Continuing to increase ω next produces a whip region followed by another whirl-like region. The predicted running speeds for the upper-speed whirl-whip transitions are different for increasing speed versus decreasing speed. As with Figure 8(b), Figure 9 predicts that V_{tL} and V_{tR} are different and not zero within the apparent whirl regimes. Generally, V_{tL} (RCl_L=125) is greater than V_{tR} (RCl_R=100).

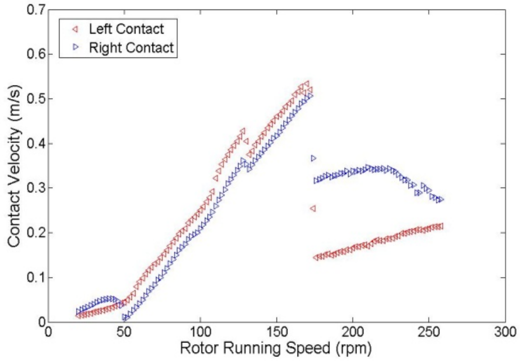

Figure. 9 Vt vs ω Speed Increasing

Overhung Disk; RCl_L= RCl_R=100

Figure 10(a) shows the major *BP* frequencies versus ω for speed increasing for both contacts. Both contacts appear to be whirling until they transition to whip at ω=56 rpm, with whip frequency 81Hz. This is close to the pinned bounce-mode natural frequency of 82.4Hz. As speed increases the right contact continue to whip at this frequency; however, at ~62 rpm the left contact appears to whirl briefly before shifting to the whip frequency 111Hz, which is close to the pinned pitch-mode natural frequency 113Hz. At ~140rpm, it reverts to whirl-like behavior. Neither the Mode-1 nor Mode-2 analytical solutions come close to predicting these outcomes.

Figure 10(b) presents predicted results for speed decreasing, showing both contact points whirling at higher speeds and shifting to whip around 90 rpm. The same whip frequencies are predicted for ω increasing and ω decreasing. Space does not permit presentation of the contact velocity predictions; however, the right contact always slips. The left contact has zero velocity during the low-speed whirl-like region. Generally, V_{tR} is greater than V_{tL} .

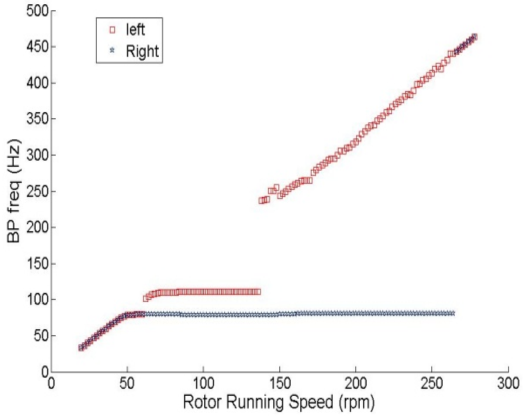

Figure. 10(a) Simulation Results (BP Freq vs Increasing speed)

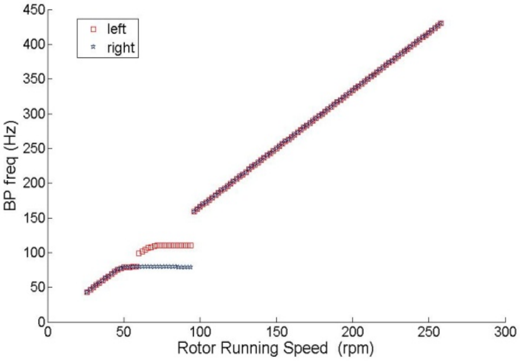

Figure. 10(b) Simulation Results (BP Freq vs Decreasing speed)

Overhung Disk; RCl_L= 100, RCl_R=125

Figure 11(a) presents predictions of *BP*s versus ω for speed increasing, showing trends similar to those of Figure 11(a) for equal *RCl* values. The left contact (RCl_L=100) whips at 81Hz over a wider speed range than the right contact that is whipping at 111 Hz. Motion at both contacts shift (separately)to whirl-like motion at higher speeds. In the upper whirl-like regions, note the lower slope for the left contact (RCl_L=100) versus the right contact (RCl_R=125). Figure 11(b) presents the speed-decreasing predictions, showing similar behavior but a broader upper-speed-range for whirl-like motion.

Space does not allow for their presentation; however, for the increasing-speed case of figure 11(a), V_{tR} is always greater than zero (slipping continuously), is always greater than V_{tL}, and increases steadily with increasing ω. V_{tL} is greater than zero except for the upper end of the higher-speed whirl-like region

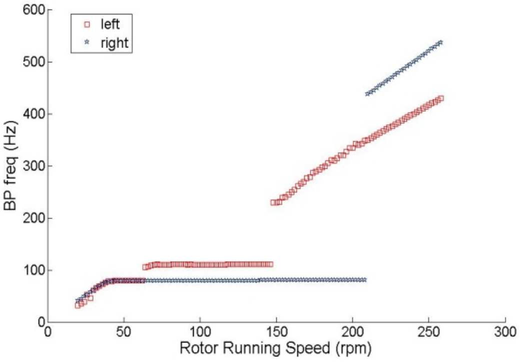

Figure. 11(a) Simulation Results (BP Freq vs Increasing speed)

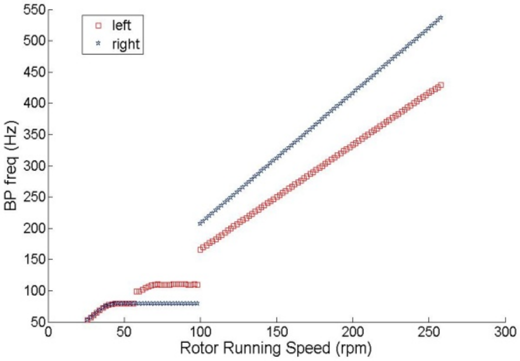

Figure. 11(b) Simulation Results (BP Freq vs Decreasing speed)

Overhung Disk; RCl_L=125, RCl_R=100

Results for this case are quite similar to those of figure 11 and are not presented. Full details may be found in Kumar [14].

SUMMARY, CONCLUSIONS, AND DISCUSSION

Dry-friction whip and whirl solutions have been developed for a rigid-rotor/rigid-stator model with contacting at two rub locations. A similar model with an elastic rotor, an elastic stator and nonlinear interaction forces has been examined using time-transient nonlinear simulations. The analytical model consists of a rigid rotor connected to an elastically-supported rigid stator at two rotor-stator rubbing-contact locations. This rigid-rotor/rigid-stator model is consistent with the low speed and low vibration frequencies observed by Clark et al. (2009). Following Black's 1968 procedure, analytical solutions can only be developed if both contact locations have the same radius to clearance (*RC*L) ratio. Analytical solutions were developed for: (1) Normal reaction forces in phase at two contacts (mode-1 solutions) , and (2) Normal reaction forces out of 180° out of phase at two contacts (mode-2 solutions). The solutions define precession-frequency regions where dry-friction whirl is possible plus indicating boundaries between whirl and whip. They resemble Black's 1968 U-shaped solutions. Analytical solutions were considered for physical models with the following mass C.G. locations: (1) centered in the stator, (2) displaced at a 3/4 position but within the contact locations, (3) overhung outside the contact locations.

The flexible-rotor/flexible-stator model with nonlinear connections at the bearings used by Wilkes et al. was employed to examine the existence of the predicted solutions, and (when they exist) more correctly establish the range of possible solutions. The nonlinear connections at the rub surface are modeled using Hunt and Crossley's model with Coulomb friction. The rotor is prescribed to rotate at a constant velocity. Simulations were performed for the rotor configurations cited above with equal and different *RCL*s at the two contact points.

Wilkes et al. (2009) found that measured experimental results and numerical predictions were in general accordance with Black's analytical model for 1-point rubbing contact as extended by Childs and Bhattacharya (2007). Their experimental results agreed well with nonlinear simulations including different running-speed transitions from whirl-to-whip during run-up and run-down operations (as analytically explained by Jiang et al. (2010)).

The central questions here are:

1. When do the predicted analytical solutions exist?
2. When they do exist, how well do they agree with predictions from the nonlinear simulations?
3. How similar/different are the phenomena for rubbing at one-contact locations and 2-contact locations?

Note: The analysis only generates predictions for the same *RCL* ratios at the two contact locations. For these conditions, the analytical solutions and the nonlinear simulations agree to some extent with the mass C.G. at centered and ¾ location in both the whirl-to-whip transition speeds and the whip frequencies (speed increasing) for the mode-1 solutions. Attempts to produce mode-2 nonlinear time-transient solution were unsuccessful. For the overhung mass case, the nonlinear simulation predicts *whip* at different frequencies for the two contact locations. Neither the mode-1 or mode-2 analytical solution predicts this outcome.

For different *RCL* ratios, nonlinear predictions for models with different *RCl* values at the contact locations produces whirl-like behavior that mimics "classic" whirl associated with rolling without slipping. For the overhung model with different *RCls*, apart from whipping at different frequencies, the two contacts also whirl at different frequencies reasonably corresponding to the *RCl* at the respective contacts. Neither of these phenomenon arise for dry-friction whip/whirl due to rubbing at one contact location

Simulations predicting transitions from whirl-to-whip in an increasing running-speed mode show different transition running speeds than those obtained in a decreasing running speed mode for whip-to-whirl for increasing speed as observed and predicted by nonlinear simulations by Wilkes et al.

Dry-friction whip and whirl occur rarely in real machines. The first author has personally known only two cases including the anemometer cited in [12]. However, they can occur, and the present analysis *predicts*: (1) "Whirl-like" behavior can arise with continuous slipping for rubbing at two-contact locations, (2) Separate supersynchronous tracking frequencies can occur simultaneously for some rotor configurations, and (3) Separate whip frequencies can occur simultaneously. Test results are needed to evaluate these 2-contact simulation predictions.

REFERENCES

[1] Newkirk, B., 1926, "Shaft Rubbing," Mech. Eng., **48**, pp. 830–832.

[2] Black, H., 1967, "Synchronous Whirling of a Shaft Within a Radially Flexible Annulus Having Small Radial Clearance," Proc. Inst. Mech. Eng, Paper No. **4** (181), pp. 65–73.

[3] Black, H., 1968, "Interaction of a Whirling Rotor with a Vibrating Stator across a Clearance Annulus," J. Mech. Eng. Sci., **10**(1), pp. 1–12.

[4] Crandall, S., 1990, "From Whirl to Whip in Rotordynamics," *IFToMM Third Intl. Conf. on Rotordynamics,* Lyon, France, pp. 19–26.

[5] Lingener, A., 1990, "Experimental Invesigation of Reverse Whirl of a Flexible Rotor," *IFToMM Third Intl. Conf. on Rotordynamics*, Lyon, France, pp. 13–18.

[6] Choi Y-S., 2002, "Investigation on the Whirling Motion of Full Annular Rub," J. Sound Vib., **258**(1), pp. 191–198.

[7] Bartha, A., 2000, "Dry Friction Backward Whirl of Rotors," Dissertation ETH No. 13817, ETH Zurich.

[8] Yu, J. J., Goldman, P., and D. Bently, 2000, "Rotor/Seal Experimental and Analytical Study of Full Annular Rub," *Proc. of ASME IGTI Turboexpo 2000*, ASME, New York, Vol. 2000-GT-389, pp. 1–9.

[9] Childs, D. and A. Bhattacharya., 2007, "Prediction of Dry-Friction Whirl and Whip between a Rotor and a Stator," ASME J. Vib. Acoust., **129**, pp. 355–362.

[10] Wilkes, J., Dyck, B. J., Childs, D., and S. Phillips, 2009, "The Numerical and Experimental Characteristics of Multi-Mode Dry-Friction Whip and Whirl, " *ASME J. for Gas Turbines and Power*, May 2010, **132**(5), pp 052503 1-9

[11] Hunt, K.., and F. Crossley, 1975, "Coefficient of Restitution Interpreted as Damping in Vibroimpact," ASME J. Appl. Mech., **42**, pp. 440.

[12] Clark, S., Clay, H., Goglia, J.A., Hoopes, T.R., Jacobs, and R. Smith, 2009, "Investigation of the NRG #40 Anemometer Slowdown," *American Wind Energy Association, Windpower 2009***,** Chicago, IL, pp. 1-16.

[13] Kärkkäinen, A., Helfert, M., Aeschlimann, B., and A. Mikkola, 2008 "Dynamic Analysis of Rotor System With Misaligned Retainer Bearings," ASME J. Tribol. **130,** 02110

[14] Kumar, D., "Backward Precessional Whip and Whirl for a Two-Point Rubbing Contact Model of a Rigid Rotor Supported by an Elastically Supported Rigid Stator," M.S. Thesis, department of Mechanical Engineering, Txas A&M University, August 2010.

[15] Childs, D., 1993, *Turbomachinery Rotordynamics: Phenomena, Modeling, and Analysis,* John Wiley and Sons, New York*,* pp. 395-431, Chap7.

[16] Wilkes, J., 2007 "A Perspective on the Numerical and Experimental Characteristics of Multi-mode Dry-friction Whip and Whirl," M.S. Thesis, Texas A&M, College Station, TX.

[17] Jiang, J., Shang, Z-Y, and L. Hong, 2010,"Characteristics of dry friction backward whirl --- A self-excited oscillation in rotor-to-stator contact systems,' Science in China Series E:Technological Sciences, **53** (3), pp. 674-683